Solid Freeform Fabrication 2024: Proceedings of the 35th Annual International Solid Freeform Fabrication Symposium – An Additive Manufacturing Conference
Reviewed Paper

Rapid Process Parameter Development for SS316L on the Freemelt ONE Open Architecture Electron Beam Powder Bed Fusion Machine

Berkay Bostan[1], Dylan Treaster[2], Daniel Ju[3], Diederik Schlingemann[3], Yanen Huang[3], Shlok Desai[3], William Frieden Templeton[3], Justin P. Miner[3], Sneha Prabha Narra[3]

[1]Department of Mechanical Engineering & Materials Science, University of Pittsburgh, PA 15261
[2]Department of Materials Science and Engineering, Carnegie Mellon University, Pittsburgh, PA 15213
[3]Department of Mechanical Engineering, Carnegie Mellon University, Pittsburgh, PA 15213

Abstract

This parameter development study for the electron beam powder bed fusion process was conducted by graduate students as part of a 4-week final project in a semester-long additive manufacturing laboratory class (24-633/27-701/39-603) at Carnegie Mellon University. The objective is to develop deposition parameters for SS316L on the Freemelt ONE electron beam powder bed fusion machine within four weeks, using only one build. An analytical model was used in conjunction with established defect criteria and process conditions for the laser powder bed fusion process to rapidly develop an initial set of process parameters - power, velocity, and hatch spacing. The results, which focus on processing defects, demonstrate the effectiveness of analytical modeling-based strategy in defining acceptable process parameters for the electron beam powder bed fusion process by using established process parameters in the laser powder bed fusion process. Further refinement is necessary to eliminate residual defects and optimize microstructure.

1 Introduction

Electron Beam Powder Bed Fusion (EB-PBF) technology has been in use for nearly 25 years, but only recently have open architecture machines and the ability to work with a wide range of materials become accessible. In contrast, laser powder bed fusion (L-PBF) has seen extensive research and development, with numerous studies exploring the use of various materials such as titanium alloys, nickel-based superalloys, and stainless steels [1], [2]. Substantial knowledge presents an opportunity to leverage the advancements in L-PBF for accelerated process parameter development in EB-PBF. This could potentially expand its material capabilities.

One of the primary challenges in EB-PBF is managing preheat parameters to avoid "smoking," a phenomenon where fine metal powders are repelled by electrostatic forces, leading to defects and ultimately fabrication or equipment failure [3], [4]. Studies have shown that controlling the temperature during preheating of the powder bed can significantly mitigate smoking, emphasizing the importance of this pre-melting step [3], [4], [5], [6]. After preheating, the focus of parameter development shifts to melting conditions. This involves selecting beam power, scan velocity, layer thickness, hatch spacing, and beam spot diameter to avoid processing defects such as porosity and excessive melting. This work focuses on developing a methodology

to choose the initial melting parameters while the preheat condition is held constant at what is believed to be a temperature that will not cause smoking.

Optimizing the melting parameters such as beam power, scan velocity, layer thickness, hatch spacing and beam spot diameter is vital in the EB-PBF process, as these parameters directly influence defect formation and overall part quality. Inadequate process parameters can lead to common defects such as lack of fusion (LoF), where insufficient energy causes incomplete melting of the powder, and keyhole-like porosity, where excessive energy creates deep, unstable melt pools [7], [8]. By carefully adjusting these parameters, it is possible to minimize these defects.

A process window defines the range of parameters, like beam power and scan velocity, that result in high-quality materials by optimizing factors such as density, microstructure, and surface quality. In L-PBF, the process window is governed by parameters such as laser power, scanning velocity, hatch spacing, layer thickness, and beam spot size, which influence defect formation like keyhole, LoF, and balling. Modeling approaches, such as defect structure process maps, normalized model-based diagrams, and data-driven models like Gaussian process regression, help predict optimal parameters and minimize defects, ensuring consistent fabrication of dense parts [9], [10]. Extensive research has focused on optimizing the processing window to minimize defects, streamline parameter development, and reduce time and cost but primarily for L-PBF. These efforts encompass various approaches, from basic geometric models to advanced microstructural simulations. Examples of these approaches include a printability metric based on the process parameter space for L-PBF, using finite element simulations to predict melt pool dimensions and identify defect-free regions for various alloys, which was validated through experimental comparisons [11]. Another approach is to use simulations based on the Eagar-Tsai model, and single-track experiments to optimize laser power and speed for achieving high-density parts in additive manufacturing [12]. A simpler approach uses a geometry-based simulation to predict LoF porosity in powder bed fusion by inputting parameters like hatch spacing, layer thickness, and melt pool cross-sectional dimensions, validating their predictions against experimental data and demonstrating the model's accuracy in identifying process conditions that lead to porosity [13]. Building on these established approaches and considering the artificially imposed build time constraints in this course project, this work aims to transfer knowledge from L-PBF using simple geometrical and mathematical predictions that do not require advanced simulations, thus enabling rapid parameter development.

This study focuses on establishing process parameters for the Freemelt ONE EB-PBF machine using stainless steel SS316L. To do this, we first examined the process settings of the EOS M290 L-PBF machine for the same material and used the beam spot size-based volumetric energy density approach to develop comparable parameters for EB-PBF. Multiple samples with a cube geometry were fabricated with varying melting conditions along the build direction to rapidly assess their impact on porosity, surface roughness, and dimensional accuracy. The results provide insights into optimizing power, velocity, and hatch spacing for a given layer thickness and beam spot size to minimize porosity and ensure maximum relative part density.

2 Methodology

2.1 Process parameter development

2.1.1 Conversion of L-PBF parameters using spot size-based volumetric energy density

Although prior research exists on process parameter development for EB-PBF manufactured SS316L components [14], [15], further investigation is essential, particularly in the development of process parameters based on more direct measures such as hatch spacing (*H*), beam power (*P*), and scanning velocity (*V*). This approach is critical for facilitating comparisons with commonly used L-PBF process. The challenge arises from the fact that exact process parameters are not always disclosed, complicating the establishment of a baseline. To address this, beam spot size (*f*)-based Volumetric Energy Density (*VEDf*), defined in Equation 1, is employed to determine the process settings. Additionally, a layer thickness (*L*) of 70 μm is used to be comparable to conventional EB-PBF settings, although lower ranges are now possible.

$$VEDf = \frac{P}{VfL}[J/mm^3] \quad (1)$$

The primary aim involves applying the same normalized Volumetric Energy Density ($\eta VEDf$) utilized in the L-PBF process to the EB-PBF process, where η is the absorptivity of the energy source to determine the energy input conditions. It is important to note that in L-PBF the laser absorptivity is typically found to be 40% for SS316L, while in EB-PBF the absorptivity is estimated to be upwards of 85% [16], [17]. This methodology requires calibrating the EB-PBF process to mirror the $\eta VEDf$ values established in L-PBF. In this context, the standard process parameters of the EOS M290, a commonly employed L-PBF machine, for SS316L, are utilized as a starting point. These parameters are detailed in Table 1. Despite the manufacturer's assertion of a laser focus diameter around 100 μm [18], prior characterization data suggests a closer approximation to an 80-90 μm range [18]. For the purposes of this study, the laser spot size is estimated to be 85 μm. Further insights into the process settings for SS316L in the L-PBF process are elaborated in [19], [20], [21]. Table 2 lists process conditions that are held constant.

Table 1. Process parameters for SS316L in the EOS M290 L-PBF machine at CMU.

P [W]	V [m/s]	L [um]	H [um]	T [°C]	f [um]	η [-]	VED_f [J/mm3]
244	1.128	40	90	27	85	0.4	63.62

Table 2. Known process parameters in the Freemelt ONE EB-PBF machine at CMU.

L [um]	T [°C]	f [um]	η [-]	ηVED_f (Requirement)	H [um]
70	750	255	1	25.44	125

After establishing the known L-PBF and EB-PBF process parameters, six distinct *P-V* combinations were derived. These developed parameters are outlined in Table 3. The strategy for selecting these six distinct *P-V* combinations involves incrementally increasing the melting rate along the build direction. Starting with lower *V* and progressing to higher *V* is crucial because, as *V* increases at the same *VEDf*, the energy transferred to the unit volume per unit time decreases, which could potentially cause issues such as porosity and melt pool instability. To ensure the possibility of a successful build, the process begins with the lowest *P-V* combination and progresses to the highest. It is noteworthy that even at the same speed as L-PBF (1.128 m/s), the beam power required for the EB-PBF process is significantly higher—while the beam power in the L-PBF process is 244 W, it increases to 512 W in EB-PBF, primarily due to the larger beam spot size and layer thickness. Other process settings were methodically determined by increasing the scanning velocity by 25% increments starting with the nominal at 1.128 m/s. Consequently, the final derived *P-V* combinations span a range of velocities from 1.128 to 2.538 m/s and a beam power range from 512 to 1153 W. The process parameter settings were designed to vary along the Z direction in every fifteen layers. This means that each 1.05 mm segment of the sample's height, consisting of fifteen layers, was printed using different *P-V* combinations, as illustrated in Fig. 1.

Table 3. Derived P-V combinations for the Freemelt ONE EB-PBF Machine. The *V* multiplier indicates the scale-up factor of the scanning velocity for the related *P-V* combination. The scanning velocity equals 1.28 times the *V* multiplier.

V multiplier [-]	V [m/s]	P [W]
1	1.128	512
1.25	1.41	641
1.5	1.692	769
1.75	1.974	897
2	2.256	1025
2.25	2.538	1153

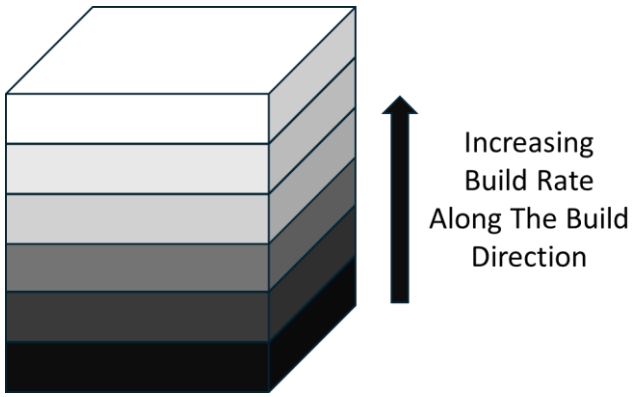

Figure 1. Sample rendering showing increasing build rate along the build direction.

2.1.2 Confirmation of VEDf-based parameters using LoF criterion

Energy density criterion is not always sufficient to confirm dense parts as it is seen that for the same energy density as varying beam power and velocities, part density is not consistent [22].To verify the *VEDf* approach, a simple geometric model proposed by Tang *et al.* [13] was used to confirm that the selected parameters are within the process window for PBF and will not undergo LoF-porosity based upon melt pool depth (*D*), width (*W*), *H*, and *L* [13]. For this case, we assume the shape of the melt pool is semi-circular leading to LoF criterion in Equation 2.

$$(\frac{H}{W})^2 + (\frac{L}{D})^2 \leq 1 \quad (2)$$

This equation indicates that a value equal to or less than 1 will have sufficient melt pool overlap, thus having no LoF porosity. This study fixed *H* and *L*, as seen in the *VEDf* approach but the melt pool width and depth must be approximated. Again, turning to Tang *et al*. [13], the authors adopted an analytical solution to determine melt pool dimensions. Instead, the closed form solution that was proposed is followed in equation 3. The melt pool width and depth solution simplified from the Rosenthal Equation is as follows:

$$D \approx \frac{1}{2}W \approx \sqrt{\frac{2Q}{e\pi\rho C(T-T_0)V}} \quad (3)$$

where Q is the absorbed beam power (ηP), C is specific heat capacity, ρ is material density, T is melting temperature, and T_0 is the preheat temperature. In our case, it was assumed that absorbed beam power is 100% which is an overestimate, but as shown in Fig. 2, both 90% and 100% assumed absorption lies well within the LoF criteria. The value used for specific heat capacity is 460 J/kg-K obtained from Mills [23]. *L*, *H*, and T_0 were set constant at 70 μm, 125 μm, and 1023 K respectively. Going through the above calculations and plotting equation two as *L/D* vs. *H/W* will reveal a relationship of a circular arc where values within the arc would avoid LoF effects and anything outside the arc could undergo LoF. This approach confirms our VEDf approach and should ensure full overlapping of melt pools to ensure a dense structure. The calculated melt pool depth based on 100% and 90% absorption equates to be 212.78 μm and 201.86 μm, respectively.

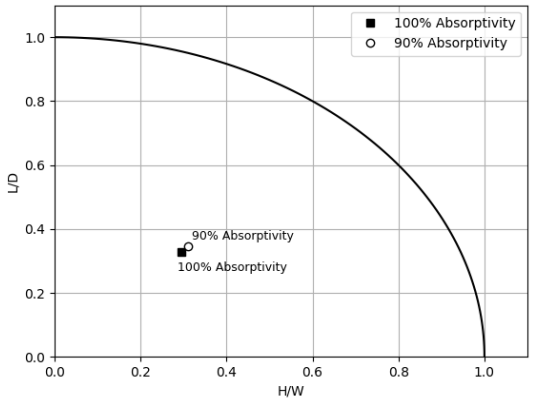

Figure 2. The processing map of hatch spacing and layer thickness, relative to melt pool geometry at assumed absorptivity levels of 90% and 100%.

2.2 Fabrication

2.2.1 Material

SS316L is a low carbon austenitic steel widely used in industries such as aerospace, medical, automotive, and marine due to its high corrosion resistance and high strength. The SS316L powder feedstock used in this work was sourced from Carpenter Additive. Table 4 presents the material composition as listed by the manufacturer [24]. The particle size distribution ranged from a minimum diameter of 45 μm to a maximum of 105 μm as stated by the manufacturer's technical specification. It should be noted that the manufacturers particle size distribution was assumed to be correct and therefore was not verified via a sieve or other similar methods. Additionally, the base plate used in this study is also SS316L supplied by Freemelt.

Table 4. SS316L composition provided by the manufacturer.

	Fe	**Cr**	**Ni**	**Mo**	**Mn**	**Si**	**N**	**O**	**P**	**C**	**S**
Min.	Bal.	16	10	2							
Max		18	14	3	2	1	0.1	0.1	0.045	0.03	0.03

2.2.2 Experimental setup

The Freemelt ONE machine was utilized for EB-PBF process in this study. It also is intended for research and development as it only has a 100 mm diameter build plate, and completely customizable parameter settings for experimental flexibility. The goal of fabricating simple geometric objects, specifically cubes, with the Freemelt ONE is to increase the success rate of construction. The design involves building six samples, each measuring 15 mm x 15 mm x 6.3 mm and spaced 20 mm apart perpendicular to the recoating rake, and 12mm apart parallel to the recoating rake, on a 100 mm-diameter build plate as shown in Fig. 3. The process parameters (*P-V*) are gradually varied along the vertical build direction in every fifteen layers of these samples based on the above criteria.

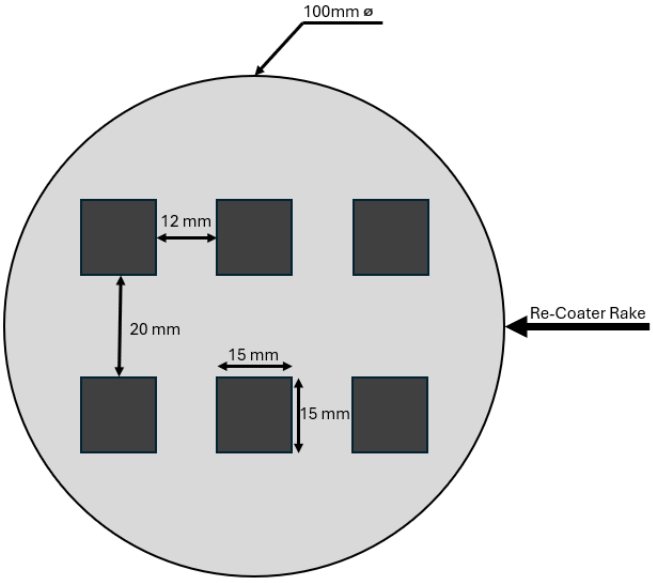

Figure 3. Build plate set up with six samples on a 100mm diameter outline of the build plate.

After printing, the top surface topography of the samples was analyzed using the Keyence VR-6200 machine, which helped determine the geometry, surface roughness, swelling, and geometric dimensions of the cubes. Different parameters (*P*-*V*) were applied to each layer to observe changes in the microstructure. Sectioning of each sample reveals the internal sections for easier examination. Each sample was bisected from the center using wire electrical discharge machining (EDM) cutting vertically from one side to the middle of the other. To remove all pieces from the construction plate, the bottom section of each element was cut along the top surface of the base plate, removing approximately 0.5 mm of the initial bottom layer. This allowed for further analysis using X-ray micro computed tomography (X-μCT) and optical microscopy after mounting and polishing.

Subsequently, the components were prepared for inspection with an optical microscope and a scanning electron microscope (SEM). Mounting was carried out using a Buehler SimpliMet 3000 Automatic Mounting Press and then polishing was done using Buehler AutoMet. Electroetching was conducted using a 10 wt.% Oxalic acid solution to help identify melt pool dimensions and microstructural features in optical micrographs. An FEI Quanta 600 FEG SEM was employed to further examine and verify porosity and cracks in the printed components. SEM imaging was conducted using a secondary electron detector, while scanning parameters were varied around 15.0kV and 500x magnification while searching for defects, and up to 1,000x magnification when evaluating individual cracks. Lastly, X-μCT was used to capture 3D porosity distribution. A scan was conducted at 160 kV and 10W using the HE18 filter on a Zeiss Crystal CT. The source to sample distance was 40.4 mm and the sample to detector distance was 565 mm resulting in a voxel size of 5 μm. A total of 1601 projections were taken consisting of 5 frames exposed for 3 seconds each. The Zeiss reconstruction software was utilized for reconstruction and segmentation and visualization was performed using Dragonfly Pro as conducted in the authors' prior work [9], [25].

3 Results and Discussion

3.1 Surface profilometry

Figure 4 shows the resulting build and the distortion in all six fabricated samples, with the center of samples being the most elevated and distorted compared to other regions. Specifically Sample 5 experienced higher amounts of super elevation and surface roughness when compared to other samples on the build plate. Melting in each layer started with melting Sample 5 and a potential lag when switching between preheat and melting conditions could have caused excess melting in Sample 5 that accumulated across different layers and resulted in more defects. Further, the build design also did not include contour scans which typically lowers surface roughness [26].

Using a Keyence VR-6200, images were acquired at the top of the surfaces to quantify the distortion. Figure 5 shows Sample 6 as a reference, as other samples had similar profiles. Micron-scale roughness is observed along the blue and yellow lines on the top surface, either horizontally or vertically, when viewed from above. These lines are then 2D mapped as shown in Fig. 5, where the yellow vertical line corresponds to the top map and the blue horizontal line corresponds to the bottom map. A color topological heat map is also provided in Fig. 5 to show the extent of bulging at the center.

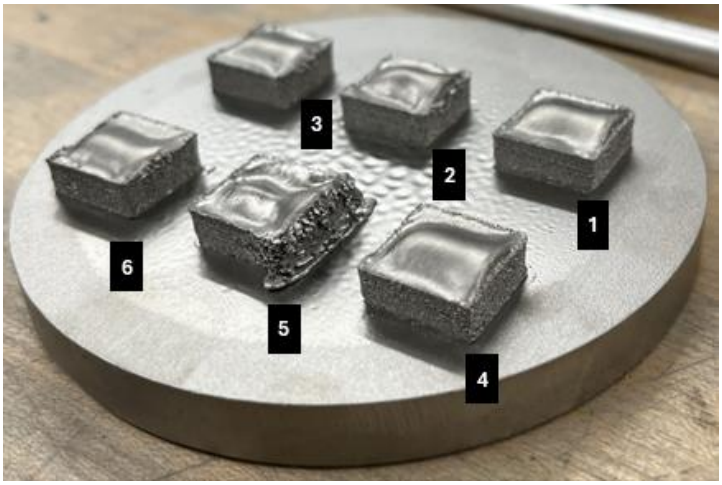

Figure 4. Photograph of the build plate with samples after cleaning the powder. The intended sample dimensions were 15 mm x 15 mm x 6.3mm.

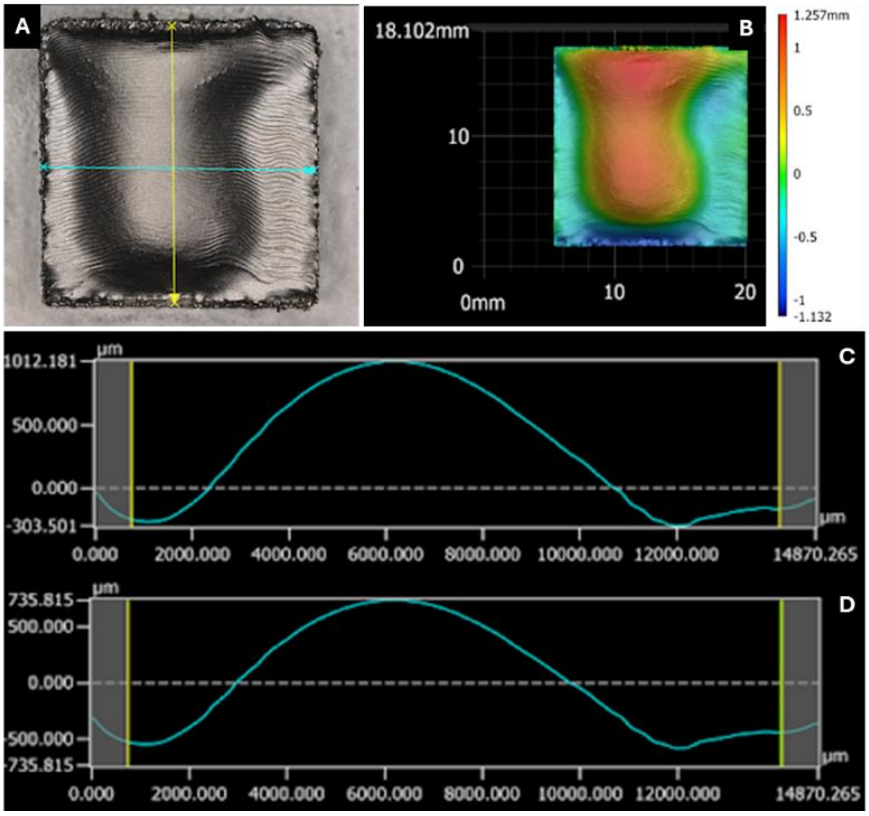

Figure 5. (a) Optical image of Sample 6, with the blue horizontal line indicating the height profile shown in image (c) and the yellow horizontal line corresponding to the height profile in image (d). (b) Color heat map illustrating the variation in height across the sample.

3.2 Optical microscopy

As shown in Fig. 6, high surface roughness around the edges is observed. The absence of contour scans is likely the main reason for this issue. Furthermore, several large pores and a microcrack have been observed around the edges. For example, the highlighted pore at the Left-3 micrograph in Fig. 6 has a length of 77 µm, and its width varies between 28-61 µm. Other pores and microcracks around the edges can be seen in the circled regions. It is also worth mentioning that the surface roughness around the edges slightly increases in the Z direction from bottom to top in Fig. 6. The main reasons for this could be that increasing the speed and beam power caused more inconsistency in the shape and melt pool stability or the large bulging in the center of the sample caused issues at the edges. At the very top, the edge surface roughness is significantly lower; it is believed that because remelting does not occur at the top layer, less inconsistency occurred and better surface quality was achieved.

Considerable porosity was not observed using optical microscopy. However, at the top of the part, three pores that are very close to each other can be seen as shown in the C-TOP micrograph in Fig. 6. Their equivalent spherical diameters are 33 µm, 21 µm, and 13.6 µm, respectively. It is also important to note that almost all pores were found in the top region in this specific cross-sectional micrograph. There is a need to conduct 3D characterization to generalize this observation for the entire sample, discussed in Section 3.3.

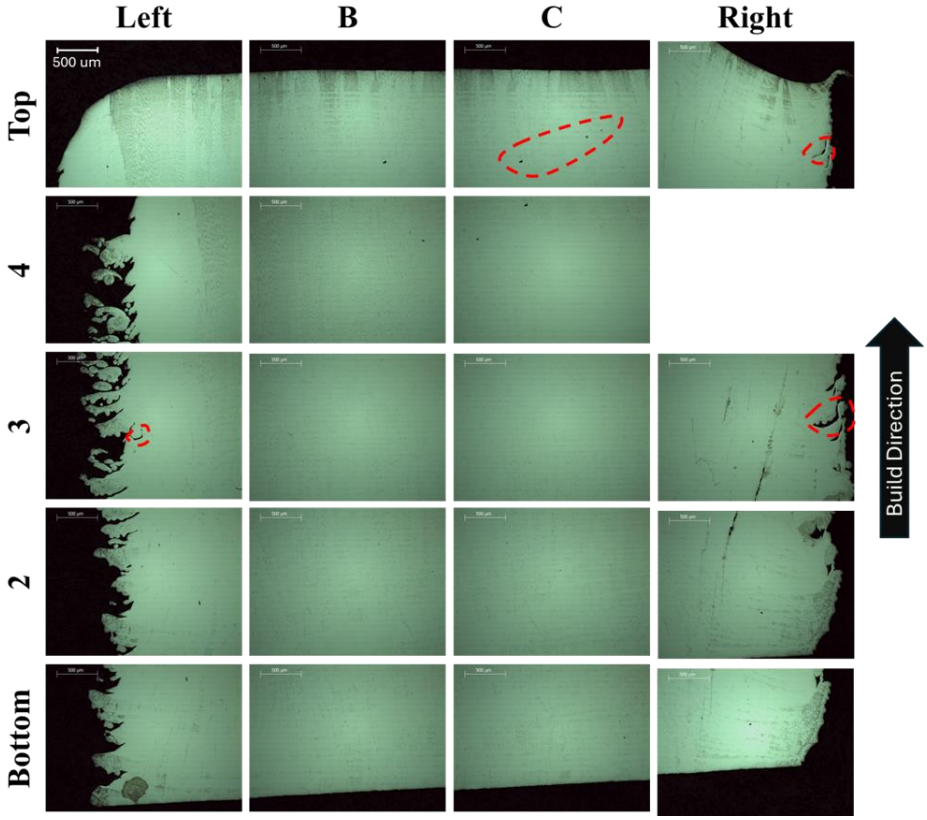

Figure 6. Cross sectional micrographs arranged from bottom to top and from left to right, showing the same section of a sample. The empty slot shows a missing section from the analysis.

Another point worth mentioning is that although parts manufactured using EB-PBF do not have considerable residual stresses [27], and previous research has shown that 3D-printed SS316L tends to distort rather than crack during the manufacturing process [28], [29]. Yet, a crack that is approximately 300 µm in length was observed in the top right region of the part, as shown in Fig. 7. This crack was initially detected in optical microscopy imaging, then verified by SEM. It is also clear from the SEM image that the crack has connected small pores to each other, indicating that it could be a porosity-induced and propagated crack. This finding indicates that porosity is one of the main challenges to be addressed during the printing process, as even the smallest pores could potentially initiate and propagate cracks.

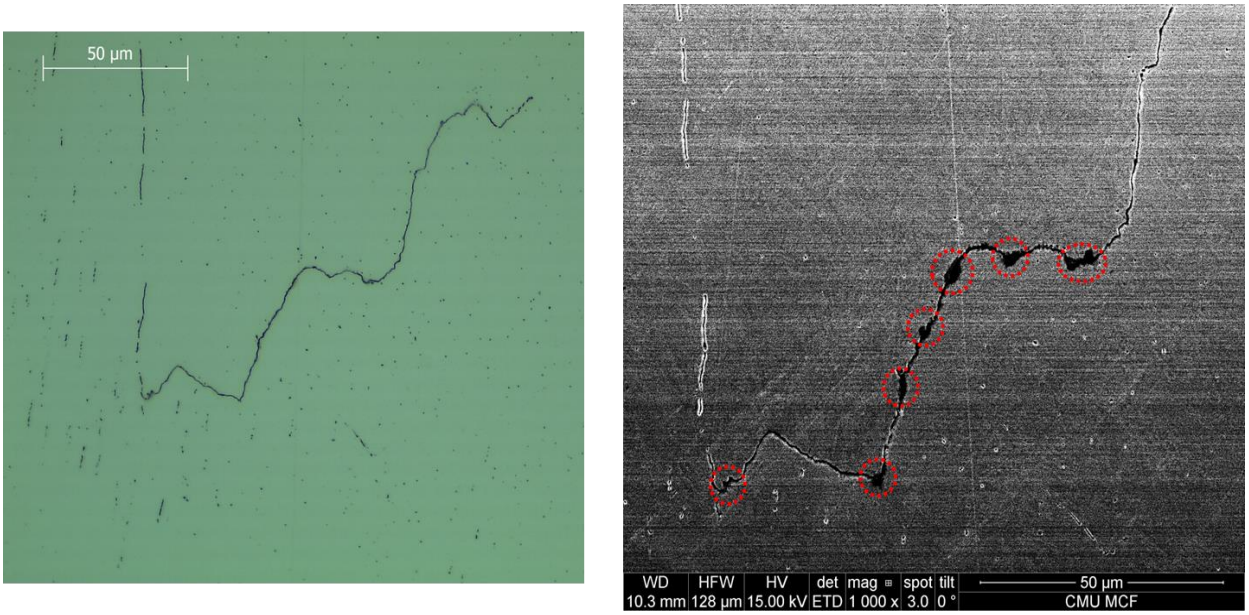

Figure 7. Optical microscopy (left) and SEM (right) images of the porosity and microcrack. Potential keyhole-like pores that may have caused crack initiation and propagation are encircled.

Optical microscopy images were also utilized to estimate melt pool dimensions and layer thickness using ImageJ (Fiji) [30]. Figure 8 shows the topmost layer as well as a representative lower layer and Table 5 details corresponding measurements from these layers. Intuitively, the reason the layers below the topmost layer are smaller is because of the remelting of layers as the print progresses. In Fig. 8, example melt pools are outlined. These melt pool widths and shallow depths are also recorded in Table 5. However, the melt pool width in this case is smaller than the actual width since the full melt pool is overlapped by the other melt tracks. The depth measurement is also from a remelted region, so it is not the actual depth measurement. Hatch spacing was also determined from the deepest part of two neighboring melt pool depths. It is also important to note that these melt pool dimensions are not statistically significant due to the small sample size (7 measurements) relative to the total number of melt pools in the entire build. However, it does provide insight into the approximate melt pool geometry in the build. These melt pool measurements were also taken at the bottom of the sample which corresponds to processing conditions in the first row in Table 3.

Table 5. Measured dimensions from the sample cross section.

	Topmost Layer Height (µm)	Lower Layer Height's (µm)	Melt Pool Width (µm)	Melt Pool Depth (µm)	Hatch Spacing (µm)
Average	255	38	124	22	125
Std Dev	12	10	7	1	5

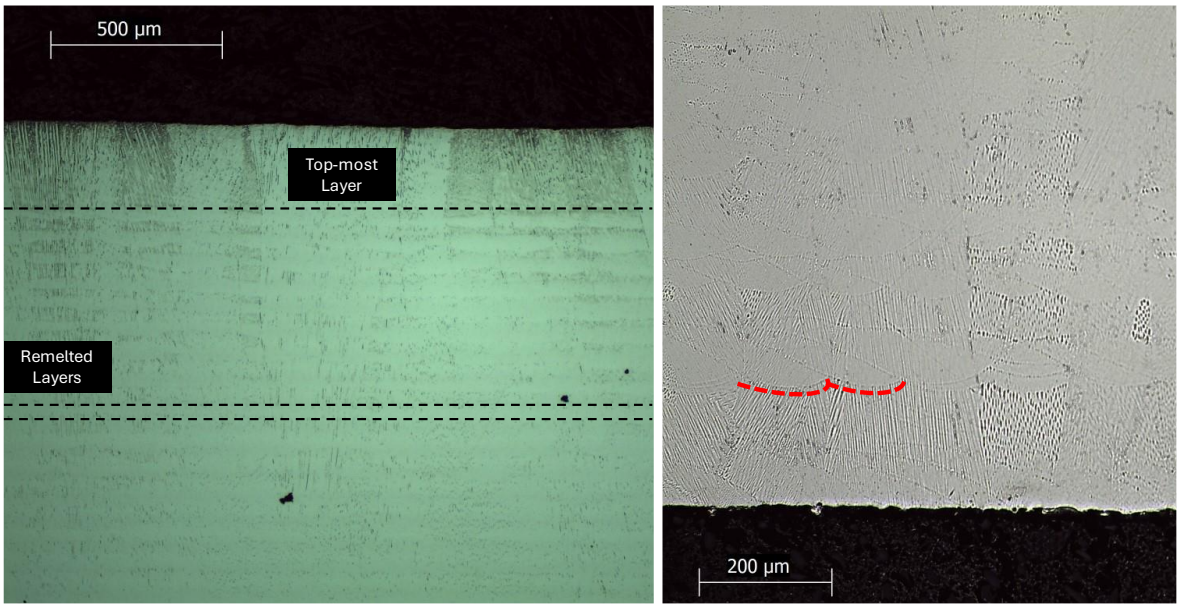

Figure 8. Top region of an electroetched sample (left). Bottom region of an electroetched sample used to measure melt pool width and depth along with hatch spacing (right). The red line highlights example melt pools.

Data in Table 5 indicates that remelted layers had an average of thickness of 38 µm, except the parameters were set to have a 70 µm layer thickness. A potential explanation is based on powder packing and consolidation. Powder packing is approximately 50%, so when the powder melts and solidifies, it is expected to shrink. In this case, the powder is assumed to pack approximately 54% efficiently based on the ratio of the observed layer thickness to the set layer thickness. The next piece of information that can be extracted is the topmost layer height which is measured to be approximately 255 µm which would correspond to the full depth of the melt pool as it's the last layer printed. This is higher than the Rosenthal-based melt pool prediction of 200 µm. This also shows that the melt pool reaches a depth that is nearly three times the set layer thickness, which may suggest that the layer thickness could be increased which would also increase efficiency. The observed adequate overlap of melt pools suggests that they are sufficiently fused, and that LoF was avoided as planned for. Additionally, there is no indication of keyhole melt pools or keyhole pores.

3.3 X-ray micro computed tomography

Figure 9 shows the distribution of porosity along the part, with the minimum pore size set to 20 µm equivalent spherical diameter (ESD) and a maximum of 150 µm. ESD of a pore is the diameter of a sphere that has the same volume as the pore. Table 6 provides details on the porosity distribution along the build direction, as well as their average, maximum pore sizes and their counts. The height thresholds along the Z direction are denoted as Z-min and Z-max. To account for an approximate 0.5 mm removal due to EDM cutting and geometrical inaccuracies, the first region spans from 0.5 to 1 mm, with subsequent regions increasing by 1 mm each in height along the build direction. As shown in Fig. 9, there is a notable increase in porosity along the build direction, particularly intensifying around the upper left edge of the part where microcrack was observed (Fig. 7). The increase in porosity along the build direction suggests that higher *P*-*V* settings led to unfavorable conditions during the build, resulting in porosity formation.

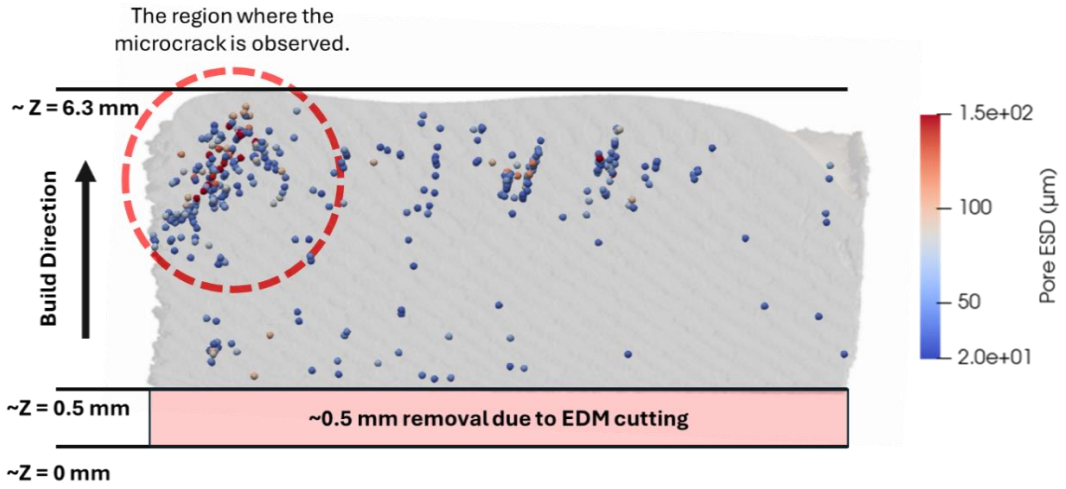

Figure 9. Porosity distribution from X-µCT characterization.

As shown in Table 6, there is an increase in porosity count, as well as their average and maximum ESD, along the Z direction with increasing *P* and *V* settings. The average pore size varies between 26.84-36.39 µm and the maximum pore size between 56.09-124.01 µm up to a height of 4 mm. Beyond 4 mm, the average pore size increases to 41.98 µm between 4-5 mm build heights, and further to 46.15 µm after 5 mm height. Moreover, the maximum pore size more than doubles, increasing to 257.7 µm and 247.0 µm, respectively. In regions with excessive porous defects, the process used 2.256 and 2.538 m/s scanning velocity, with 1025 and 1153 W beam power (Fig. 1). It is possible that the increased *P* and *V* as well potential changes to the layer thickness due to accumulation of excess melting regions were unable to properly melt the powder layer, leading to large LoF porosity, particularly evident in the 320 porosity defects in the region of 4-5 mm height. Additionally, it is worth noting that the number of pores, as well as their average and maximum sizes, decreased between 2-3 mm height, where 769 W beam power and 1.692 m/s scanning velocity were used. This suggests a potential optimal location in the process space where the powder layer is melted more effectively, resulting in a smaller number of pores and reduced pore sizes.

Table 6. Porosity measurements along the build direction.

Z-min [mm]	Z-max [mm]	Number of Pores	Average ESD [μm]	Maximum ESD [μm]
0.5	1	22	34.67	100.58
1	2	78	33.01	101.60
2	3	40	26.84	56.09
3	4	115	36.39	124.01
4	5	320	41.98	257.70
5	-	134	46.15	247.14

4 Conclusions

This study, conducted as part of the class project of the 24-633/27-701/39-603 Additive Manufacturing Laboratory course at Carnegie Mellon University, aimed to rapidly develop process parameters for SS316L using the Freemelt ONE EB-PBF machine within a single machine run and a 4-week time frame, by characterizing a single printed sample cube. Unlike L-PBF, process parameter development for EB-PBF has recently gained increased attention, even though EB-PBF has been utilized for over two decades. This shift is likely due to the recent availability of the open architecture EB-PBF machines in the recent years.

The primary objective of this study is to transfer knowledge from L-PBF to EB-PBF, thereby expediting process development. To achieve this, we derived a simple analytical model based on the VEDf. This model effectively converted known L-PBF process parameters to EB-PBF by adjusting power and velocity using VEDf normalized by beam absorptivity. Six different *P*-*V* combinations were derived, ranging from lower to higher settings, with power and scanning velocity increasing by 25% increments along the build direction every fifteen layers during the printing process. Since VEDf does not account for hatch spacing, the developed processing parameters were also validated using geometrical LoF porosity criterion.

Following the printing process, surface profilometry, optical microscopy, and X-μCT porosity analyses were conducted to assess the properties of the part across different regions printed with varying parameters. The porosity analysis revealed a trend of increasing porosity with higher *P*-*V* particularly when the power exceeded 1 kW, and the velocity surpassed 2.25 m/s. In these regions, a substantial increase in porosity was observed, potentially leading to the formation of a microcrack in the top left region of the part, likely initiated during the cooling phase and exacerbated by the propagation of a microcrack that connects the pores. However, the study also demonstrated that increasing power and velocity did not universally degrade part quality. At a power of 769 W and a velocity of 1.692 m/s, the number of pores was significantly lower among the conditions tested.

Acknowledgements

The authors wish to express their gratitude to Carnegie Mellon University for offering and supporting 24-633/27-701/39-603 Additive Manufacturing Laboratory course in Spring 2024. This course enabled the students to manufacture and characterize the builds with the resources provided by the NextManufacturing Center and Materials Characterization Facility supported by grant MCF-677785. Special thanks to Doug Washabaugh, additive manufacturing technician, for managing the lab safely and efficiently.

Additionally, the X-Ray Micro Computed Tomography Machine was funded by the Army Research Laboratory Cooperative Agreement Number W911NF-20-2-0175. The views and conclusions contained in this document are those of the authors and should not be interpreted as representing the official policies, either expressed or implied, of the Army Research Laboratory or the U.S. Government. The U.S. Government is authorized to reproduce and distribute reprints for Government purposes notwithstanding any copyright notation herein.

References

[1] W. Abd-Elaziem *et al.*, "On the current research progress of metallic materials fabricated by laser powder bed fusion process: a review," *J. Mater. Res. Technol.*, vol. 20, pp. 681–707, Sep. 2022, doi: 10.1016/j.jmrt.2022.07.085.

[2] S. Chowdhury *et al.*, "Laser powder bed fusion: a state-of-the-art review of the technology, materials, properties & defects, and numerical modelling," *J. Mater. Res. Technol.*, vol. 20, pp. 2109–2172, Sep. 2022, doi: 10.1016/j.jmrt.2022.07.121.

[3] D. Wang, D. Zhao, X. Liang, X. Li, and F. Lin, "Multiple stages of smoking phenomenon in electron beam powder bed fusion process," *Addit. Manuf.*, vol. 66, p. 103434, Mar. 2023, doi: 10.1016/j.addma.2023.103434.

[4] C. Körner, "Additive manufacturing of metallic components by selective electron beam melting — a review," *Int. Mater. Rev.*, vol. 61, no. 5, pp. 361–377, Jul. 2016, doi: 10.1080/09506608.2016.1176289.

[5] M. Larsson and A. Snis, "Method and device for producing three-dimensional objects," US 8,187,521 B2, May 29, 2012.

[6] G. Rizza, M. Galati, and L. Iuliano, "A phase-field study of neck growth in electron beam powder bed fusion (EB-PBF) process of Ti6Al4V powders under different processing conditions," *Int. J. Adv. Manuf. Technol.*, vol. 123, no. 3–4, pp. 855–873, Nov. 2022, doi: 10.1007/s00170-022-10204-4.

[7] E. Bol, G. M. Kelley, and M. Ramulu, "Characterisation of defects following MicroCT sampling inspection of specimens produced by electron beam powder bed fusion," *Virtual Phys. Prototyp.*, vol. 19, no. 1, p. e2384660, Dec. 2024, doi: 10.1080/17452759.2024.2384660.

[8] S. Aota *et al.*, "Solidification behavior and porosity in electron-beam powder bed fusion of Co–Cr–Mo alloys: Effect of carbon concentrations," *Addit. Manuf.*, vol. 59, p. 103134, Nov. 2022, doi: 10.1016/j.addma.2022.103134.

[9] T. Reddy *et al.*, "Fatigue-based process window for laser beam powder bed fusion additive manufacturing," *Int. J. Fatigue*, vol. 187, p. 108428, Oct. 2024, doi: 10.1016/j.ijfatigue.2024.108428.

[10] A. Rausch, V. Küng, C. Pobel, M. Markl, and C. Körner, "Predictive Simulation of Process Windows for Powder Bed Fusion Additive Manufacturing: Influence of the Powder Bulk Density," *Materials*, vol. 10, no. 10, p. 1117, Sep. 2017, doi: 10.3390/ma10101117.
[11] L. Johnson *et al.*, "Assessing printability maps in additive manufacturing of metal alloys," *Acta Mater.*, vol. 176, pp. 199–210, Sep. 2019, doi: 10.1016/j.actamat.2019.07.005.
[12] C. Kamath, B. El-dasher, G. F. Gallegos, W. E. King, and A. Sisto, "Density of additively-manufactured, 316L SS parts using laser powder-bed fusion at powers up to 400 W," *Int. J. Adv. Manuf. Technol.*, vol. 74, no. 1–4, pp. 65–78, Sep. 2014, doi: 10.1007/s00170-014-5954-9.
[13] M. Tang, P. C. Pistorius, and J. L. Beuth, "Prediction of lack-of-fusion porosity for powder bed fusion," *Addit. Manuf.*, vol. 14, pp. 39–48, Mar. 2017, doi: 10.1016/j.addma.2016.12.001.
[14] Z. Fu and C. Körner, "Actual state-of-the-art of electron beam powder bed fusion," *Eur. J. Mater.*, vol. 2, no. 1, pp. 54–116, Dec. 2022, doi: 10.1080/26889277.2022.2040342.
[15] C. Wang, X. Tan, E. Liu, and S. B. Tor, "Process parameter optimization and mechanical properties for additively manufactured stainless steel 316L parts by selective electron beam melting," *Mater. Des.*, vol. 147, pp. 157–166, Jun. 2018, doi: 10.1016/j.matdes.2018.03.035.
[16] W. E. King *et al.*, "Observation of keyhole-mode laser melting in laser powder-bed fusion additive manufacturing," *J. Mater. Process. Technol.*, vol. 214, no. 12, pp. 2915–2925, Dec. 2014, doi: 10.1016/j.jmatprotec.2014.06.005.
[17] "GE Additive_EBM_White paper." GE Additive. [Online]. Available: https://go.additive.ge.com/rs/706-JIU-273/images/GE%20Additive_EBM_White%20paper_FINAL.pdf.
[18] "SDS EOS M 290." EOS GmbH. Accessed: Apr. 10, 2024. [Online]. Available: https://www.eos.info/en-us/metal-solutions/metal-printers/data-sheets/sds-eos-m-290.
[19] A. Evangelou *et al.*, "Effects of process parameters and scan strategy on the microstructure and density of stainless steel 316 L produced via laser powder bed fusion," *J. Alloys Metall. Syst.*, vol. 3, p. 100027, Sep. 2023, doi: 10.1016/j.jalmes.2023.100027.
[20] M. Gor *et al.*, "A Critical Review on Effect of Process Parameters on Mechanical and Microstructural Properties of Powder-Bed Fusion Additive Manufacturing of SS316L," *Materials*, vol. 14, no. 21, p. 6527, Oct. 2021, doi: 10.3390/ma14216527.
[21] S. Theeda, S. H. Jagdale, B. B. Ravichander, and G. Kumar, "Optimization of Process Parameters in Laser Powder Bed Fusion of SS 316L Parts Using Artificial Neural Networks," *Metals*, vol. 13, no. 5, p. 842, Apr. 2023, doi: 10.3390/met13050842.
[22] H. Gu, H. Gong, D. Pal, K. Rafi, T. Starr, and B. Stucker, "Influences of energy density on porosity and microstructure of selective laser melted 17-4PH stainless steel," *Solid Free. Fabr Symp Proc Austin 2013*, pp. 474–489.
[23] K. Mills, Recommended Values of Thermophysical Properties for Selected Commercial Alloys. Woodhead Publishing, 2002.
[24] "PowderRange_316L_Datasheet.pdf." Carpenter Additive. [Online]. Available: https://www.carpenteradditive.com/datasheet-powderrange-316l.
[25] *Dragonfly*. Comet Technologies Canada Inc, Montreal, Canada. [Online]. Available: https://www.theobjects.com/dragonfly
[26] Z. Ren, "On the role of pre- and post-contour scanning in laser powder bed fusion: Thermal-fluid dynamics and laser reflections," *Int. J. Mech. Sci.*, 2022.

[27] D. Xie *et al.*, “A Review on Distortion and Residual Stress in Additive Manufacturing,” *Chin. J. Mech. Eng. Addit. Manuf. Front.*, vol. 1, no. 3, p. 100039, Sep. 2022, doi: 10.1016/j.cjmeam.2022.100039.
[28] J. Kluczyński *et al.*, “Crack Growth Behavior of Additively Manufactured 316L Steel—Influence of Build Orientation and Heat Treatment,” *Materials*, vol. 13, no. 15, p. 3259, Jul. 2020, doi: 10.3390/ma13153259.
[29] N. Chen *et al.*, “Microstructural characteristics and crack formation in additively manufactured bimetal material of 316L stainless steel and Inconel 625,” *Addit. Manuf.*, vol. 32, p. 101037, Mar. 2020, doi: 10.1016/j.addma.2020.101037.
[30] J. Schindelin *et al.*, “Fiji: an open-source platform for biological-image analysis,” *Nat. Methods*, vol. 9, no. 7, pp. 676–682, Jul. 2012, doi: 10.1038/nmeth.2019.